Princeton Plasma Physics Laboratory

PPPL-5197

Initial experimental test of a high density plasma mass filter

R Gueroult, E S Evans, S J Zweben, N J Fisch
Princeton Plasma Physics Laboratory, Princeton University, Princeton, NJ 08543 USA
F Levinton
Nova Photonics, Inc, Princeton, NJ, 08540, USA

September 2015

Prepared for the U.S. Department of Energy under Contract DE-AC02-09CH11466.

Princeton Plasma Physics Laboratory
Report Disclaimers

Full Legal Disclaimer

Trademark Disclaimer

PPPL Report Availability

Princeton Plasma Physics Laboratory:

http://www.pppl.gov/techreports.cfm

Office of Scientific and Technical Information (OSTI):

http://www.osti.gov/scitech/

Related Links:

U.S. Department of Energy

U.S. Department of Energy Office of Science

U.S. Department of Energy Office of Fusion Energy Sciences

Initial experimental test of a high density plasma mass filter

R Gueroult, E S Evans, S J Zweben, N J Fisch

Princeton Plasma Physics Laboratory, Princeton University, Princeton, NJ 08543 USA

F Levinton

Nova Photonics, Inc, Princeton, NJ, 08540, USA

Abstract.

High throughput plasma mass separation requires rotation control in a high density multi-species plasmas. A preliminary mass separation device based on a helicon plasma operating in gas mixtures and featuring concentric biasable ring electrodes is introduced. Plasma profile shows strong response to electrode biasing. In light of floating potential measurements, the density response is interpreted as the consequence of a reshaping of the radial electric field in the plasma. This field can be made confining or de-confining depending on the imposed potential at the electrodes, in a way which is consistent with single particle orbit radial stability. Concurrent spatially resolved spectroscopic measurements suggest ion separation, with heavy to light ion emission line ratio increasing with radius when a specific potential gradient is applied to the electrodes.

1. Introduction

The potential of plasmas to separate elements based on their mass has long been recognized, as illustrated by the development of the Calutron device [1] during the Manhattan project. Following these initial developments, the unique capabilities of rotating plasma configurations were quickly identified [2]. For instance, plasma centrifuges can operate at larger rotation speeds than their gaseous or liquid counterparts thanks to their ability to operate without moving parts. These larger rotation speeds offer in turn higher separation factor and larger processing rates [3].

Although most of the research conducted in this field has been dedicated to isotope separation [4, 5, 6], plasma based mass separation has recently been proposed for new applications, such as nuclear waste remediation [7, 8] and nuclear spent fuel reprocessing [9, 10]. These new applications differ from isotope separation in that the mass difference between the elements to be separated is large, typically a few tens of atomic mass units or more. This larger mass difference allows in principle for larger throughputs or processing rates. In this context, three different high throughput mass filter concepts based on rotating plasma configurations have been proposed [11, 12, 13]. In these filters, separation is achieved either through the existence of a mass dependent maximum rotation velocity for particle confinement[11], by balancing centrifugal and magnetic forces in an asymmetric device [12, 14], or by creating mass dependent ion trapping potential wells at different radii through sheared rotation [13].

Three common core capabilities can be identified for these three concepts. First, high throughput processing demands high density plasmas ($10^{18} - 10^{19}$ m^{-3}). Second, separation implies multiple species, so that the plasma source must handle complex plasma compositions. Third, rotation based separation requires means for plasma rotation control.

The proposed high density plasma source for these applications is a helicon source, which routinely produces plasmas in pure argon with densities equal of greater than 10^{19} m^{-3}, and that both with spiral [15] and helical [16] antennas. However, although helicon discharges in gas mixtures have been studied [17, 18], high density operation with complex plasma compositions remains to be demonstrated.

While other control means could be considered, such as waves [19], the conceptually simplest technique for plasma rotation control is electrode biasing. With a few exceptions, most of the biasing experiments in linear devices were aimed at fluctuation and transport control or suppression [20, 21, 22, 23, 24]. For such applications, the focus is on the efficiency of biasing for fluctuation control rather than on the ability to shape the potential profile. Nevertheless, modifications of the plasma profile through biasing were clearly demonstrated in this process, both in DC discharges [23, 24] and RF plasmas [21, 22]. In addition, concurrent plasma rotation information obtained by means of Mach probe measurements, when available, shows strong response to biasing. However, rotation control requires the ability not only to affect the radial potential profile, but to control it. In this regard, the ability to control the radial potential slope has been demonstrated using multiple electrodes at lower density (10^{17} m^{-3}) in an ECR plasma [25, 26].

Previous efforts aimed at demonstrating mass separation capabilities in crossed field configurations were conducted in a low density (10^{16} m^{-3}), single ion species, helicon plasma [27]. Besides, this study mainly focused on how a single positive bias at the end of the plasma affects the plasma potential and plasma rotation, and did not and attempt to impose a radial potential profile on the electrodes. However,

plasma rotation response to biasing is shown to exhibit different traits depending on the plasma composition (pure argon or pure xenon).

In this paper, we present the results of a preliminary investigation of a high throughput plasma mass filter concept development experiment. First, in Sec. 2, the preliminary device for high throughput plasma mass separation is introduced, along with the available diagnostics. In Sec. 3, characteristics of the intrinsic rotation observed in this device are reported and analyzed. In Sec. 4, plasma properties response to electrode biasing is discussed, and some explanations are proposed for the observed trends. In Sec. 5, preliminary spatially resolved spectroscopic measurements suggesting ion separation are presented. In Sec. 6, the main findings are summarized.

2. The Plasma Mass Filter eXperiment

The Plasma Mass Filter eXperiment (Pmfx) setup is shown in Fig. 1. This setup is adapted from the Spiral Antenna Helicon High Intensity Background (Sahhib) experiment [28], which was previously built and used for the development of Motional Stark Effect (MSE) with Laser Induced Fluorescence (LIF) plasma diagnostic [29, 30]. The Pmfx chamber used for these investigations is made of two distinct parts: a 30 cm in radius, 50 cm long main chamber where the plasma is formed, and a smaller, 7.3 cm in radius, 40 cm long secondary chamber in which the plasma expands. The vacuum vessel is pumped by a combination of a Pfeiffer TPU-200 turbo-pump (200 L/s pumping speed) and a Leybold Heraeus TriVac roughing pump, offering a base pressure of about 10^{-6} Torr. Two distinct gas input lines are connected to the main chamber in the machine mid-plane. One is at the edge of the machine ($r \sim 30$ cm), while the other one is inserted in the chamber and can be moved closer to axis. Pressure is measured using a combination of capacitive and ion gauges. Two set of 5 large, water cooled, coils, distant by 18.5 cm, create the axial magnetic field. In the current setup, the two coils closest to the antenna (left in Fig. 1) are left unpowered, whereas the other 8 coils are connected in series. A DC power supply (EMHP 60-500) provides a current $\mathcal{I}_c$ up to 500 A. On-axis axial magnetic field values obtained for 300 and 500 A are respectively 580 G to 950 G in the central region. For small radii ($r \lesssim 10$ cm), axial field intensity variations are limited in between the coils, but becomes significant in regions outside of each coils set.

In addition to gas injection, a dust dropper is installed on top of the vacuum chamber mid-distance between the magnetic coils as shown in Fig 1. The design of this dropper prototype is inspired by the NSTX lithium dust dropper [31], but incorporates a 178 μm mesh as the bottom of the dust container, and a small motor with an off-center weight to provide vibration. This prototype can inject 5 mg/s of 2 μm silica spheres for up to 20 minutes. In the absence of plasma, the presence of dust falling though the machine is validated visually. This is confirmed by observing dust collecting on a window at the bottom of the vacuum chamber.

An Axcelis RF power supply delivering up to 1 kW at 13.56 MHz is used for plasma generation in Pmfx. In contrast with most helicon sources which use saddle antennas, the RF energy is coupled to the plasma using a $m = 0$ planar spiral antenna [32]. The 6 cm radius spiral antenna is positioned behind a quartz window, perpendicular to the machine axis. Another peculiarity of Pmfx is that, as opposed to other helicon experiments where the plasma expands from the source to a larger chamber (for example Csdx [33], HelCat [34], Helix-Leia [35]), the secondary chamber is smaller, and, in some sense, plays the role of limiter. Various gases have

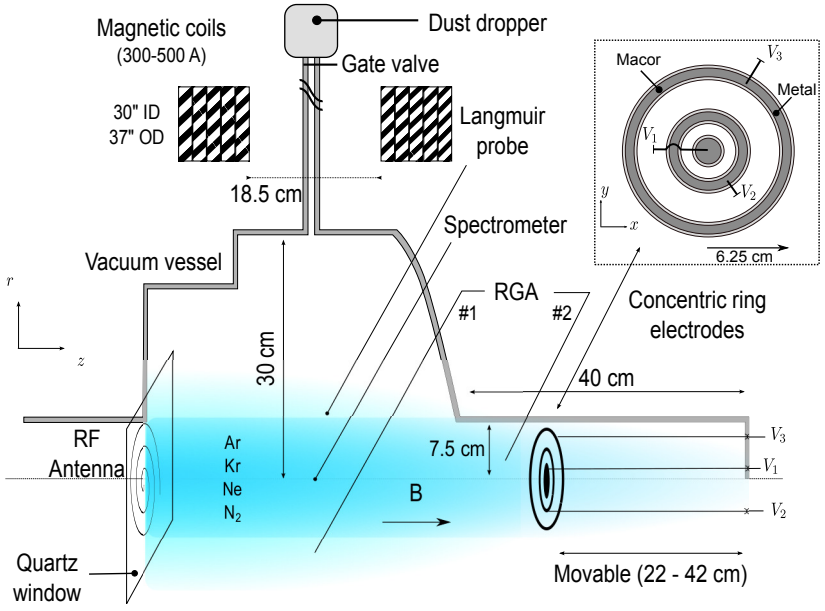

(a) Cut view in the (r, z) plane.

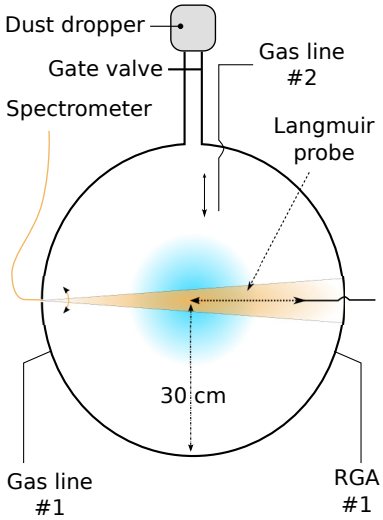

(b) Cut view in the machine mid-plane

Figure 1. Sketch of the experimental setup. Details of the three concentric ring electrodes are given to scale in the upper right corner in Fig. (a).

been tested, with successful helicon modes ($n > 10^{13}$ cm^{-3}) in Ar and Kr, as well as various gas mixtures (Ne/Ar, N_2/Ar, Ar/Kr) in various ratios. The machine can be operated continuously for about 30 min at a time, after which it has to be stopped in order for the vacuum vessel to cool down.

At the other end of the device, a set of three concentric ring electrodes faces the plasma. These three electrodes can be brought closer or moved further away from the antenna. Each of these electrodes can be biased independently with respect to the machine, and is powered using of a Lambda Genesys 100V/33A DC power supply. The central electrodes is 1 cm in radius and is covered by a 3 mm thick dielectric layer. The inner and outer electrodes are respectively 2.5 cm and 5.7 cm in radius, 1.25 cm thick, and covered inside and outside with a 3 mm thick dielectric layer. Electrodes can be removed from the device to allow for fast camera imaging of the plasma along the discharge axis. Images are acquired with a 128×128 pixel resolution at a rate of 26143 frames/s using a Phantom v7 camera. A narrow band optical filter centered on 488 nm (Ar II) is installed in front of the camera. In this setup, the obtained images correspond to measurements integrated along the line of sight.

A dual tip Langmuir probe is used to measure simultaneously the floating potential and plasma density. The probe is mounted on a translation stage to obtain radial profiles in the machine mid-plane between the coils. The probe tips are made of Tungsten and are 150 μm in radius and 10 mm long. One tip of the probe is floating and is used to measure the floating potential, while the other one is biased negatively (-25 V) to measure the ion saturation current I_{is}. Alternatively, a voltage ramp can be applied to the biased tip to record $I(V)$ curves at a given radial location. Although estimates of the electron temperature T_e can in principle be deduced from the measured $I(V)$ curve, proper T_e measurements in PMFX would require a RF compensated probe [36, 37]. Consequently, a uniform electron temperature $T_e = 3$ eV is used in this study. This value is chosen as an average based on the radial profile measurements reported in the literature for similar helicon discharges (*e. g.* [38, 39]). The ion saturation measurement I_{is} is then used to infer the local density assuming Bohm ion current [40]

$$I_{is} = I_{Bohm} = 0.6 e n_i \sqrt{\frac{kT_e}{m_i}} A_{probe}, \tag{1}$$

where n_i is the ion density, A_{probe} is the probe collecting area and e is the elementary charge. Signals are recorded using a NI-6212 acquisition card, with sampling rates of 0.4 and 20 kS/s. The Langmuir probe motion control and acquisition is automated using a python script. For some biasing conditions, the insertion of the probe within the plasma core (brightest central region) leads to a collapse of the plasma, accompanied by a large drop in density. The plasma core usually recovers as the probe is pulled out. More generally, it is not uncommon for the operating parameters to vary slightly as the probe is scanned radially. These variations suggest plasma perturbation by the probe.

A movable fiber optic cable and lens are used to capture light emission along a chord of the device. This signal is then sent to an Ocean Optics USB2000 spectrometer. In addition, a Residual Gas Analyzer (RGA) is used to analyze the gas composition as sampled from two different locations in the machine. One sampling location is on a radial port in the machine mid-plane (see Fig. 1(b)), while the other is on a radial port in the secondary chamber, close to the electrodes.

3. Intrinsic rotation

Intrinsic rotation is a relatively common feature in high density helicon discharges [41, 42, 43, 38, 21], and is observed in PMFX. Results of fast camera imaging in pure argon, obtained along the discharge axis when electrodes were removed, are shown in Fig. 2. At 3 mTorr, a $m = 2$ mode rotating in the clockwise direction, *i. e.* the ion diamagnetic direction, is clearly visible and stable over a few periods. Observation of rotation in the ion diamagnetic direction is consistent with previous results reported in helicon discharges (*e. g.* [44, 38]). In some cases, this feature was specific to the core region at high field [45]. Similar rotation direction has been observed when a limiter is applied to a DC magnetized plasma column [23, 24]. The rotation frequency in these conditions is estimated to be about 2.1 kHz (about $12 - 13$ frames per rotation at 26143 frames/s), which, again, is comparable to previously reported values [38]. Assuming visible light intensity is proportional to ion saturation current [46, 47, 39], fast camera imaging offers indirect information on the plasma density profile. Results obtained at low pressure (3 mTorr Ar) and depicted in Fig. 2 suggest a hollow profile. Experiments carried out at higher pressure (5 mTorr Ar) indicate a profile peaked on axis.

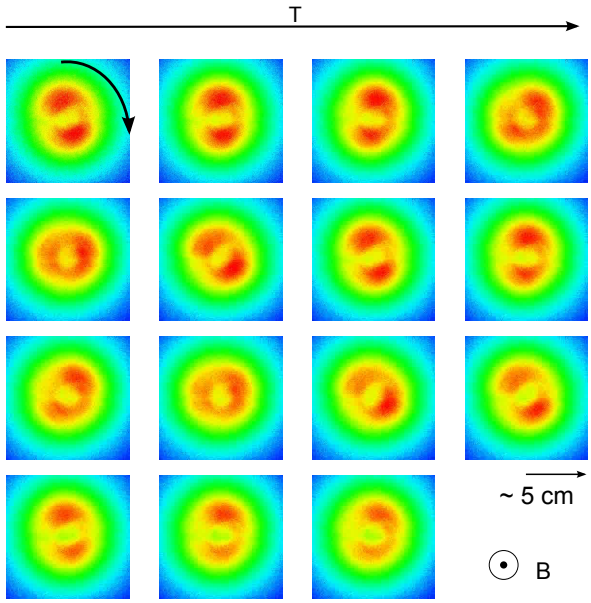

Figure 2. Frames sequence (left to right and top to bottom) illustrating intrinsic rotation in pure Ar at 3 mTorr. Rotation frequency is about 3 kHz. Light emission seems to indicate a hollow density profile. On-axis field $B \sim 580$ G and input RF power is 800 W. Frame rate is 26143 frames/s.

A more quantitative picture of the plasma rotation can be obtained by tracking light intensity variations along the azimuthal direction. For this purpose, the camera field of view is re-mapped to polar coordinates. The origin of the polar coordinates system is found by computing the weight average center as obtained by stacking a large number (~ 500) of frames. Light emission as a function of the azimuthal angle Θ can then be plotted within a given shell $r_1 < r < r_2$. For a discharge in pure argon

at 5 mTorr, the result computed for 15 mm $\leq r \leq$ 20 mm is plotted in Fig. 3. Similar patterns are obtained for 7.5 mm $\leq r \leq$ 35 mm. For these conditions, a $m = 3$ mode is observed as indicated by the three local maxima at any given time. This mode is stable over hundreds of periods. The fact that the light intensity of these maxima is not constant over the full 2π angle comes from the fact that the emission iso-contours are not strictly circular, but ellipsoid. A possible explanation for this feature might be the alignment of the spiral antenna with the magnetic coils. From the typical azimuthal revolution of these maxima, as highlighted in red in Fig. 3, the rotation frequency is 2.6 kHz.

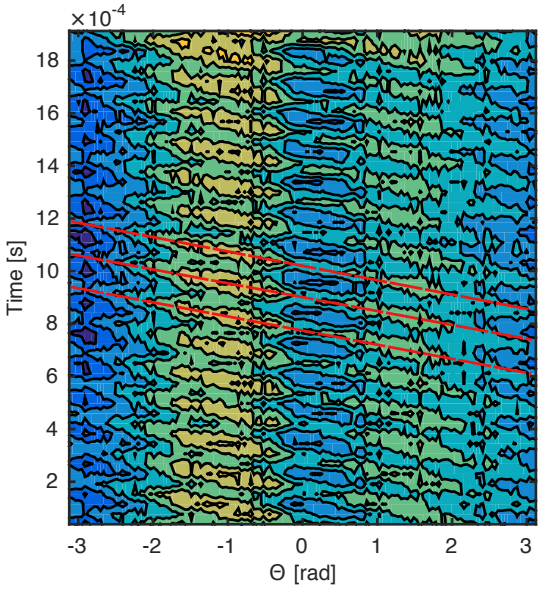

Figure 3. Time evolution of the light intensity along the azimuthal direction. Line integrated light intensity is summed on the shell 15 mm $\leq r \leq$ 20 mm. The dashed red lines highlight the trajectory in the (Θ,t) space of the three azimuthal maxima over one period. Operating conditions: 5 mTorr Ar, on-axis field $B \sim$ 580 G and 800 W.

A confirmation of this result is obtained by computing the time evolution of the light intensity fluctuations about the mean value (averaged over time) at a given azimuthal location. For this purpose, the azimuth angle is divided into 50 bins, and pixel information is averaged in each bin. The frequency response in any of these azimuthal bin can then be obtained as a function of the radial position, as depicted in Fig. 4. The power density shows a maximum for $f \sim 8.1$ kHz. Based on a $m = 3$ mode such as identified above, this yields $f \sim 2.7$ kHz. Additionally, the *FFT* indicates that the rotation frequency of this $m = 3$ mode is constant across the plasma radius, or, in other words, that this mode features solid body rotation. Finally, a lower amplitude mode, localized around $r = 1.5$ cm, is visible in the same figure.

Unfortunately, Langmuir probe measurements could not be carried out simultaneously with fast camera imaging along the discharge axis. However, Langmuir probe measurements were taken for similar discharge conditions (pure Argon at 5 mTorr, on-axis magnetic field $B \sim$ 580 G), but with the ring electrodes in the

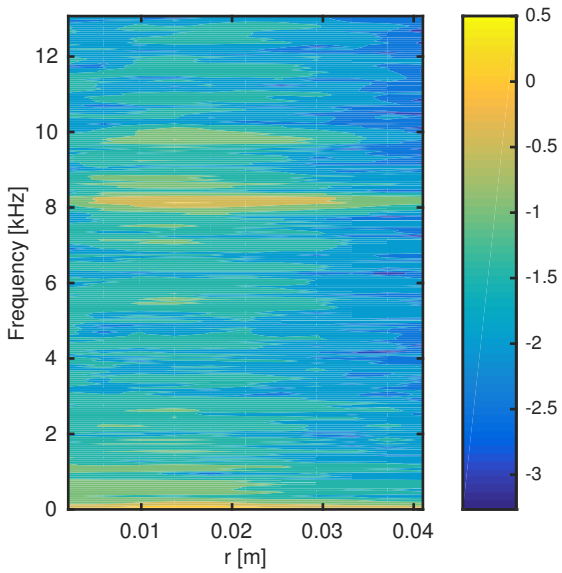

Figure 4. Space resolved light intensity fluctuation FFT spectra (log_{10}). The $m = 3$ mode at 2.7 kHz (peak at 8.1 kHz) is seen across most or the plasma radius. Operating conditions: 5 mTorr Ar, on-axis field $B \sim 580$ G and 800 W.

chamber. Although the electrodes were in this case unpowered, their presence in the chamber could possibly alter the plasma properties by modifying the boundary conditions. The density and floating potential profile measured in these conditions are plotted in Fig. 5. With the assumption of a uniform electron temperature, the plasma potential radial profile V_p follows the floating potential profile V_f, and the radial electric field in the plasma can be deduced directly from the V_f profile plotted in Fig. 5. The negative potential gradient observed in the core is consistent with the rotation direction deduced from fast camera imaging. Quantitatively, the positive electric field in this region leads to rotation frequencies $f_{E\times B} \sim E_r/(rB_z)$ of the order of 10 kHz. Since the potential decreases almost linearly in this region, the rotation frequency scales with r^{-1} to the first order. This 10 kHz estimate is about three times the solid-body rotation frequency inferred from the fast camera data. The difference between these two values might be explained in part by the diamagnetic drift, which goes against the $E \times B$ rotation in the region exhibiting a negative potential gradient. However, the corresponding frequency

$$f^\star = -\frac{k_B T_e}{2\pi r e B}\frac{\partial n}{n \partial r}, \tag{2}$$

with e the elementary charge, B the magnetic field intensity and r the radial coordinate, is about an order of magnitude lower, and hence can not fully explain the observed difference.

Moving to the positive potential gradient region ($r \gtrsim 30$ mm in Fig. 5), both the $E \times B$ drift and the diamagnetic drift are in the electron diamagnetic direction. Although the intensity of the $m = 3$ rotation mode analyzed above seems to decrease past 30 mm, no rotation in the electron diamagnetic direction was observed with the

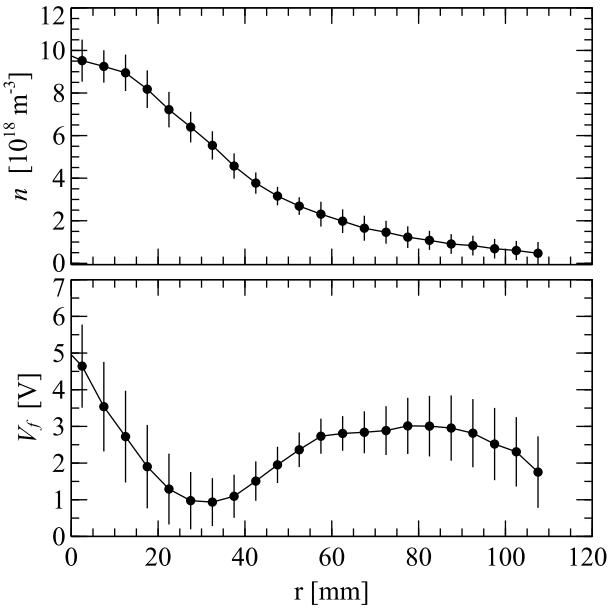

Figure 5. Density and floating potential radial profiles obtained in Ar at 5 mTorr, on-axis field $B \sim 580$ G and 800 W.

fast camera. While this difference might be the consequence of the presence of the electrodes in the chamber, another explanation is the following one. Positive potential gradient is observed in the machine-mid-plane for $r > 30$ mm. However, because of the magnetic field divergence, the plasma is expected to expand as we move away from the mid-plane. Quantitatively, for an on-axis magnetic field $B \sim 580$ G (coil current $\mathcal{I}_c = 300$ A), the magnetic surface having a radius $r = 30$ mm in the mid-plane will have a radius $r = 48$ mm about 50 cm away from the mid-plane, and already $r = 35$ mm at the axial location where the source chamber joints the smaller secondary chamber (limiter). For this reason, the rotation in the electron diamagnetic (positive) direction might not be observed far away from the mid-plane at radii visible in the camera field of view ($r \lesssim 50$ mm). Since the fast-camera data is integrated along the whole length of the plasma, and that a significant fraction of the plasma length is in the secondary chamber away from the machine mid-plane, the positive rotation from the machine mid-plane at large radii might be averaged out by negative rotation information seen further away from the machine mid-plane along the line of sight.

4. Plasma response to biasing

For the remaining of this study, the electrodes are located as far back as possible, that is to say 73 cm from the antenna. Additional experiments were performed with electrodes closer to the antenna, but maintaining a high density helicon discharge while biasing generally proved to be much more difficult in these conditions. Since our underlying objective is to evaluate mass separation effects in a rotating plasma, biasing experiments are carried out in a gas mixture. Although various gas mixtures (Ne/Ar, N_2/Ar, Ar/Kr), and species ratio, were tested, a 5 mTorr Ar, 1 mTorr Kr

gas composition is used here. Typical plasma parameters obtained in these conditions are summarized in Table 1 and Table 2 .

Property	Value
Density [m^{-3}]	10^{19}
Ionization fraction	0.1
Ion Larmor radius ρ_L [mm]	$1-10$
Electron gyro-frequency Ω_e [GHz]	2.5
Ion gyro-frequency Ω_i [kHz]	$17-36$

Table 1. Typical plasma properties in PMFX without bias for 5 mTorr Ar, 1 mTorr Kr gas composition, on-axis field $B \sim 950$ G and 800W of RF power. Ion Larmor radius is obtained for Ar^+ and Kr^+ and $0.03 \leq T_i \leq 0.1$ eV.

Interaction	Frequency [Hz]
Electron-neutral collision	$\nu_{en} \sim 10^7$
Ion-neutral collision	$\nu_{in} \sim 1-3\ 10^3$
Electron-ion collision	$\nu_{ei} \sim 10^8$

Table 2. Typical interaction frequencies for 5 mTorr Ar, 1 mTorr Kr gas composition, on-axis field $B \sim 950$ G and 800W of RF power.

When the discharge gas consists of two gas species α and β, the Bohm current contains two unknowns n_{i_α} and n_{i_β}, and

$$I_{is} = I_{Bohm} = 0.6e\sqrt{kT_e}\left(\frac{n_{i_\alpha}}{\sqrt{m_\alpha}} + \frac{n_{i_\beta}}{\sqrt{m_\beta}}\right)A_{probe}, \tag{3}$$

with $n_{i_\alpha}+n_{i_\beta} = n_e$. The relative abundance of the two ion species depends on the local plasma properties. A rough estimate of this ratio for the gas mixture considered here can be obtained using the model proposed by Bai *et al.*[48]. In this model, the relative abundance is dictated by the electron temperature, the gases relative partial pressures, and the ionization rate of each species. Using typical ionization cross sections for Ar and Kr [49], and the gas mixture considered here, $(n_{i_{Ar}}, n_{i_{Kr}})$ varies from $(0.6, 0.4)$ for $T_e = 3$ eV to $(0.75, 0.25)$ for $T_e = 10$ eV. Since the existing diagnostics do not provide an accurate measurement of the electron temperature, an average mixture species $n_{i_{Ar}}/n_{i_{Kr}} = 0.7/0.3$ is used to compute n_i from Eq. 3.

The subset of biasing conditions analyzed in this paper are summarized in Table 3. Density and floating potential profiles obtained for these biasing conditions are plotted in Fig. 6. The electrodes are biased with respect to the machine, and the inner electrode is grounded. Current drawn at the central and outer electrodes seems to follow the density profile, and varies from 0.5 to almost 2 A depending on the biases. A 1 A current is equivalent to current densities $j_c \sim 1500$ A/m^2 and $j_o \sim 400$ A/m^2 on the central and outer electrodes, respectively. Assuming an ion thermal speed $v_{i_{th}} \sim 750$ m.s^{-1} (equivalent to $T_i \sim 0.1$ eV for Ar), these current densities correspond to ion densities $n_i = j(ev_{i_{th}})^{-1}$ of respectively 1.25 10^{-19} and 3.7 10^{18} m^{-3}. Such values are consistent with the densities inferred from Langmuir probe measurements.

Comparing the density profiles in Fig. 6, the first observation is that the density on-axis is enhanced when a positive potential potential gradient is imposed on the electrodes (cases $\mathcal{B}$, $\mathcal{C}$ and $\mathcal{D}$). Conversely, the density on-axis decreases when a

Case	$\mathcal{A}$	$\mathcal{B}$	$\mathcal{C}$	$\mathcal{D}$	$\mathcal{E}$	$\mathcal{F}$
Central electrode V_1 [V]	-	-10	-10	-20	0	15
Inner electrode V_2 [V]	0	0	0	0	0	0
Outer electrode V_3 [V]	-	0	10	15	-25	-25

Table 3. Various biasing cases used in a Ar/Kr mixture (5 mTorr Ar, 1 mTorr Kr), on-axis field $B \sim 950$ G and 800 W. V_1, V_2 and V_3 are the biases respectively applied, with respect to the machine, to the central, the inner and the outer electrode (see Fig. 1). A "-" sign means an unpowered electrode.

negative potential gradient is imposed on the electrodes (cases $\mathcal{E}$ and $\mathcal{F}$). In addition, on-axis density enhancement is associated with a narrower density profile, whereas an off-axis maximum is formed as the density on-axis falls off, leading to a hollow, and much broader, profile. This limited set of biasing conditions is however not sufficient to determine whether the plasma response is mainly dictated by the potential gradient imposed between the central and inner electrodes, or between the inner and outer electrodes, or simply by the overall gradient.

Turning now to the floating potential, plotted in the lower half of Fig. 6, one sees that the general profile differs from the pure Ar case, obtained for a weaker magnetic field plotted in Fig. 5 (on-axis magnetic field of about 580 G instead of 950 G). The potential gradient past the expected zone of influence for the outer electrode ($r \gtrsim 45$ mm) is quite similar for all biases imposed on the three electrodes, and does not show the positive gradient at larger radius seen in Fig. 5. In the region where a direct influence of the electrodes is expected ($r \lesssim 45$ mm in the machine mid-plane), a more careful examination reveals two different behaviors, as highlighted in Fig. 7. On one hand, cases $\mathcal{C}$ and $\mathcal{D}$ feature a double hump profile, with a local minimum between the inner and outer electrodes, and maxima on axis and close to the outer electrode. On the other hand, cases $\mathcal{A}$, $\mathcal{E}$ and $\mathcal{F}$ show a single hump, with a maximum between the inner and outer electrodes, and a local minimum on axis. In other words, when a positive gradient is applied between the inner and outer electrodes (cases $\mathcal{C}$ and $\mathcal{D}$), a positive floating potential gradient is observed in the plasma in the region between this electrodes. Conversely, when a negative potential gradient (cases $\mathcal{E}$ and $\mathcal{F}$) is applied between this same electrodes, a negative floating potential gradient is observed in the plasma. Finally, when a zero gradient is applied between the inner and outer electrodes (case $\mathcal{B}$), the floating potential remains close to constant over a large fraction of the corresponding plasma region. No similar pattern can be seen for the bias applied between the central and the inner electrodes.

Although the sign of the floating potential gradient appear to be affected by the electrodes, at least in the region between the inner and outer electrodes, the floating potential values measured differ significantly from the ones applied on the electrodes. This is particularly true for the floating potential values measured on axis. For example, central electrodes biases of -20 and 15 V both lead to measured floating potential of about $13 - 15$ V, while biases of -10 and 0 V on this same electrode lead to on-axis floating potentials of about $8 - 10$ V. Two possible explanations can be proposed for this behavior. The first possibility is a perturbation of the plasma due to the presence of the probe, as mentioned in Sec. 2. It stands to reason that this disturbance would be maximal on axis, since this is the position for which the support of the probe protrudes into the plasma the most probe. The second

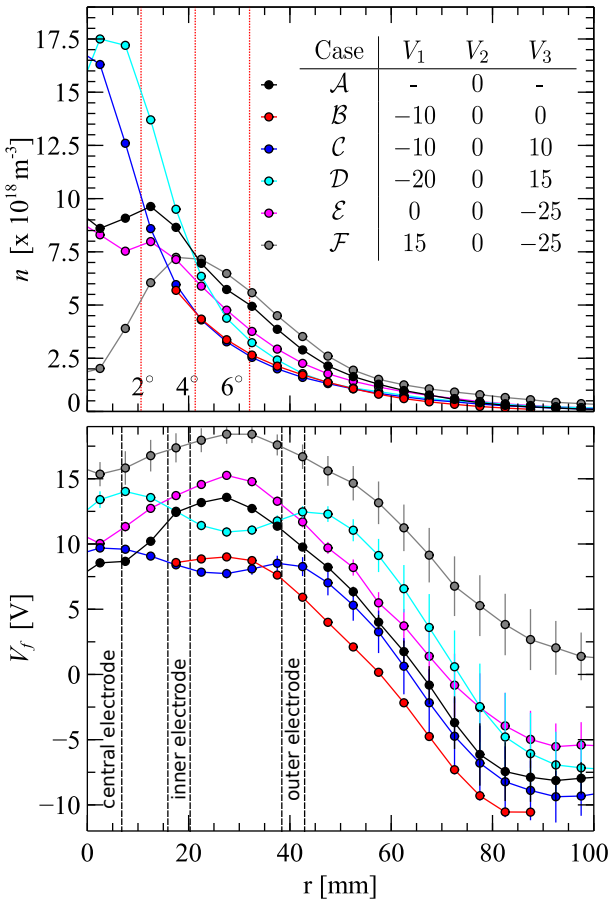

Figure 6. Density and floating potential radial profiles obtained with electrode biasing in a Ar/Kr mixture (5 mTorr Ar, 1 mTorr Kr), on-axis field $B \sim 950$ G and 800 W. V_1, V_2 and V_3 are the biases respectively applied to the central, the inner and the outer electrode (see Fig. 1). A "-" sign means an unpowered electrode. The vertical dashed lines in the lower figure represents the radial coordinates of the three electrodes projected along the field lines.

possibility is the presence of the quartz window facing the biasing electrodes. Most biasing experiments featuring helicon plasmas (with the exception of the work done by Shinohara's group [50, 51, 27]) rely on cylindrically shaped antennas that surround the plasma, so that the boundary conditions at both end of the device can be controlled. In PMFX, termination on the magnetic field lines on the quartz window on the antenna side (see Fig. 1) is likely to modify the plasma response. In this configuration, the potential along a field line is not tied to two electrodes with well defined potential, but to one electrode on one side, and to a surface of which the electric potential depends on the plasma parameters.

While a better understanding of the floating potential distribution along the field lines is a clear prerequisite for effective plasma rotation control and, in turn, mass separation, it appears that some traits of the plasma density profile response to biasing

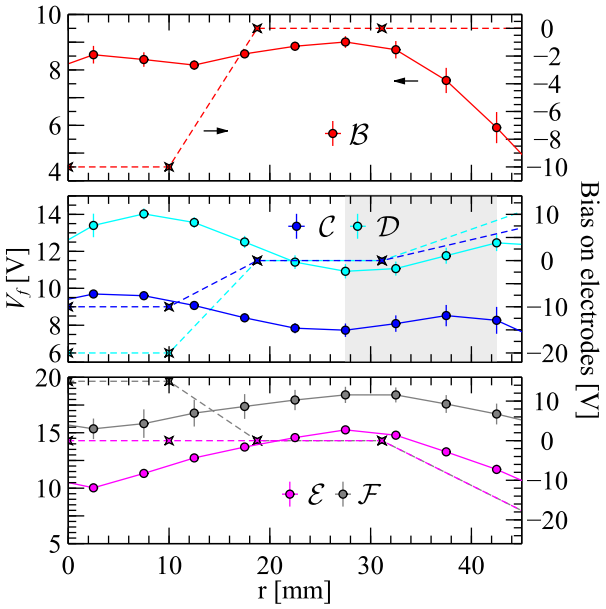

Figure 7. Floating potential radial profile in the core region along with the potential profile applied at the electrodes for various biasing cases (see Table 3). As highlighted by the grey box, floating potential increases in the region localized between the inner and outer electrodes when a positive potential gradient is applied between these same electrodes.

can already be identified as follows. When a positive potential gradient is applied on the electrodes, an enhancement of the density is observed on axis, with a larger density gradient. Simultaneously, a positive floating potential gradient V_f is observed in the plasma at a radius matching the one of the biased electrodes.

Assuming the plasma potential gradient sign will remain identical to the one of V_f (this would be the case for limited T_e variations across the plasma column), the density increase on axis can be explained in terms of the negative radial electric field E_r formed locally in the plasma. Conversely, the plasma hollowness and larger radial extent observed when a negative potential gradient is imposed at the electrodes could be explained as the consequence of the positive radial electric field formed in the plasma. As a matter of fact, single particle orbit analysis in the cross-field configuration indicates that an ion orbit is radially unstable if $E_r \geq rB_z\omega_{ci}/4$, with $\omega_{ci} = eB_z/m_i$ the ion cyclotron period. In this simple model, confinement is mass dependent, and differential effects could in principle be observed in a multi-ion species plasma such as studied here.

5. Preliminary evidence for differential effects

In order to evaluate whether the biasing effects discussed in the previous section could manifest themselves in the form of mass differential effects, emission spectroscopy measurements were carried out. The idea is to use the ratio of specific ion lines as a proxy for differential confinement effects. The preliminary diagnostic used for this

purpose relies on measuring the intensity of various pre-identified ion emission lines for Ar and Kr, integrated along a line of sight, as shown in Fig. 8. This measurement is reproduced for various angles α to probe the plasma along different chords. A sense of the radial position probed for a given angle α is given in the upper plot of Fig. 6, where the dotted vertical red lines represent the radius of the chords obtained for $\alpha = 0°, 2°, 4°, 6°$. An inverse Abel transform would allow to compare directly the ion line emission radial profile to the density radial profile obtained from Langmuir probe measurement. Unfortunately, since this chord scan is done manually, the resolution is too limited to perform a meaningful inverse Abel transform. Future experiment upgrades could remedy to this limitation.

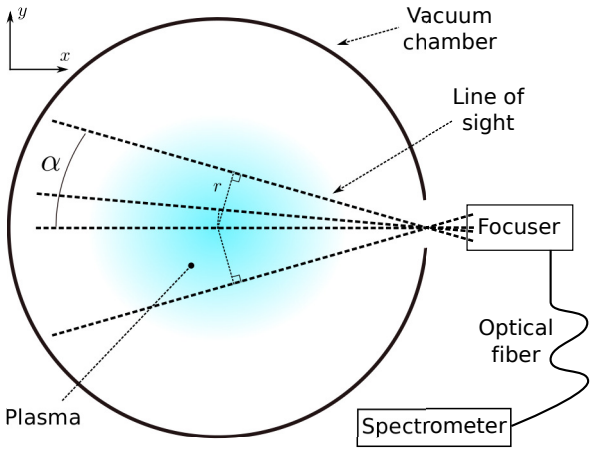

Figure 8. Sketch of the spectroscopic diagnostic for differential effects. Light emission, integrated along a given line of sight, is collected and analyzed to monitor the intensity of specific Ar and Kr ion lines as a function of the angle α.

The ion lines monitored were identified in pure Ar and pure Kr discharges, and were chosen because they are sufficiently isolated, separated and intense. Based on these criteria, the lines studied here are an Ar II line at 487.98 nm, and two Kr II lines at 481.18 and 482.52 nm. The intensity of the two Kr II lines is summed and compared to the Ar II line. The evolution of the intensity of the Ar II and Kr II lines as the line of sight is shifted off-axis is shown in Fig. 9. The first general observation is that the intensity decreases by over an order of magnitude between $\alpha = 0°$ and $\alpha \gtrsim 5°$, for all biasing cases. This result is qualitatively consistent with the density profile obtained by Langmuir probe measurements and plotted in Fig. 6. Indeed, density measurements show for most cases a decrease of the density by a factor two or more past 30 mm. These values are consistent considering that the emission intensity scales with the density squared. Now looking at the different biasing cases individually, one recovers the trends deduced from the density profile analysis. Namely, cases for which a positive potential gradient is applied at the electrodes ($\mathcal{B}$, $\mathcal{C}$ and $\mathcal{D}$) present a strong emission intensity peak on axis, which quickly falls off with α. Conversely, cases for which a a negative potential gradient is imposed on the electrodes ($\mathcal{E}$ and $\mathcal{F}$) yields a much broader emission, and even possibly a hollow profile ($\mathcal{F}$). It is worth noting that quantitative comparison of the various biasing cases is not straightforward here since one would need information on the electron temperature T_e response to biasing

to backtrace density information from relative emission intensities.

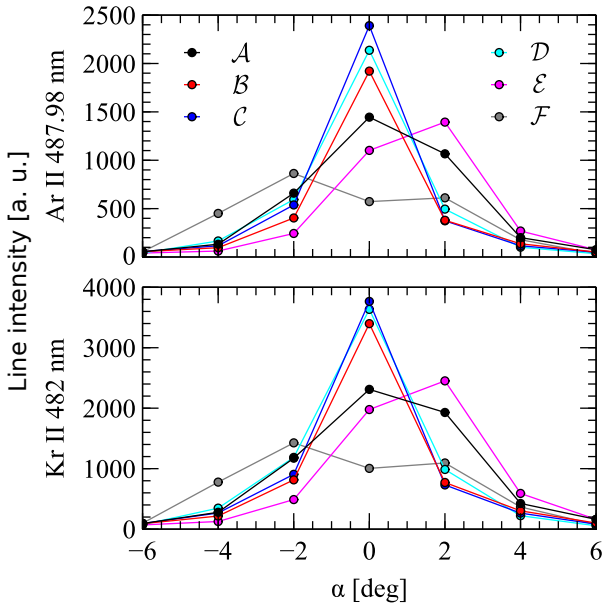

Figure 9. Line integrated line intensity as a function of the projection angle α, *i. e.* different chords, for various biasing cases. The Ar II line is at 487.98 nm; the Kr II line is at 482 nm and is the sum of two distinct Kr II lines at 481.18 and 482.52 nm.

Direct comparison of line emission profiles for Ar and Kr ions in Fig. 9 is difficult, and does not show clear differences. However, plotting the ratio of the Kr II line intensity over the Ar II line intensity as shown in Fig. 10, highlights an interesting trend. For negative radial electric field set between the inner and outer electrodes (cases $\mathcal{C}$ and $\mathcal{D}$), the ratio of line intensities peaks for $\alpha = 4°$ and then falls-off quickly. For a zero radial electric field between the inner and outer electrode (case $\mathcal{B}$), the behavior is qualitatively similar, but the decrease past 4° is less pronounced. Now, when a positive radial electric field is imposed between the inner and outer electrodes (cases $\mathcal{E}$ and $\mathcal{F}$), the ratio of lines intensities does not show a drop past 4°, but rather seems to saturate between 4 and 6°.

Although these results are preliminary, and will have to be confirmed with a larger set of measurements and improved spatial resolution, the highlighted spectral line intensity radial profile variations with biasing point to differential confinement effects. Qualitatively, a possible explanation for the observed evolution of the ion line intensity ratio is depicted in Fig. 11. When a positive radial electric field exists in the plasma, single particle orbit theory predicts larger radial oscillations for heavier particles. More specifically, ions of different mass but same charge will display different azimuthal motion due to the contribution of the centrifugal force to the drift velocity. As a result, for a given initial ion temperature, heavy ions orbit will exhibit larger radial displacements than light ones. This is illustrated by the orbits shown in Fig. 11(a), obtained for singly charged Ar and Kr ions, a magnetic field $B = 950$ G, a plasma radius $r = 10$ cm and radial electric field $E_r = 2\Phi_0 r/a^2$ with $\Phi_0 = 8$ and 10 V

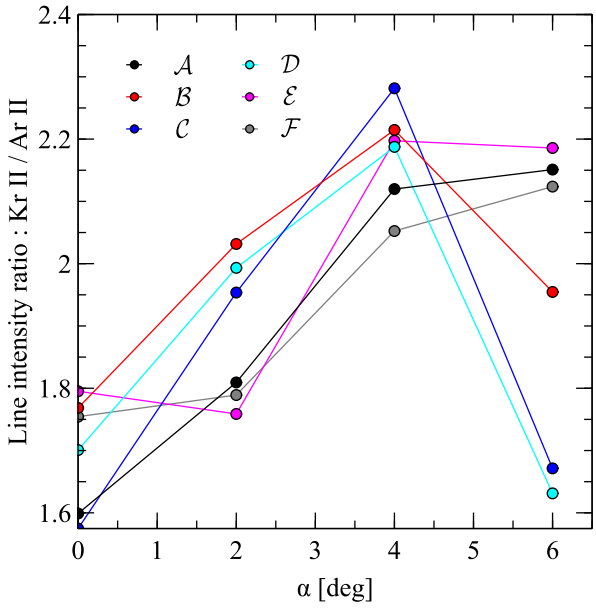

Figure 10. Ratio of Kr ion line intensity to Ar ion line intensity as a function of the projection angle α for various biasing cases. Ar II line is at 487.98 nm; Kr II line is at 482 nm and is the sum of two distinct Kr II lines at 481.18 and 482.52 nm.

the potential difference between the core and the edge of the plasma. Centrifugal effects are negligible when $E_r/(rB) \ll eB/m_i$, but become large as the angular drift velocity approaches the ion cyclotron frequency (ion radial confinement is lost for $E_r > eB^2r/(4m_i)$). Since the cyclotron frequency depends on the ion mass, these effects can be important for heavy ions (Kr^+), but, at the same time, almost negligible for lighter ions (Ar^+).

Averaging over the ion population, the radial displacement dependance on E_r would lead to a broader density profile, as highlighted for Kr^+ ions in Fig. 11(b). Because of their much smaller mass, effects on the Ar^+ ions are much less pronounced, and the argon ion density profile can be in first approximation assumed to remain unmodified. Corresponding density ratios plotted in the lower figure show very similar properties to the ion line intensity profile obtained from spectroscopic measurements. This result suggests a correlation between radial separation of ion species of different mass (Ar and Kr here) and the sign of the potential gradient imposed at the electrodes. However, this result will have to be analyzed in relation to the electron temperature T_e radial profile to differentiate effects due to T_e spatial variations from true differential confinement effects.

It is worth mentioning here that Residual Gas Analyzer (RGA) measurements did not show evidence of biasing effects. More precisely, gas composition analysis at two different locations in the device (see Fig. 1) did not show relative variations across the different elements, only global variations that can be attributed to density variations. However, since RGA measurements rely on neutral measurements, this inconclusive result could be due to various effects, such as recycling at the walls. In addition, since

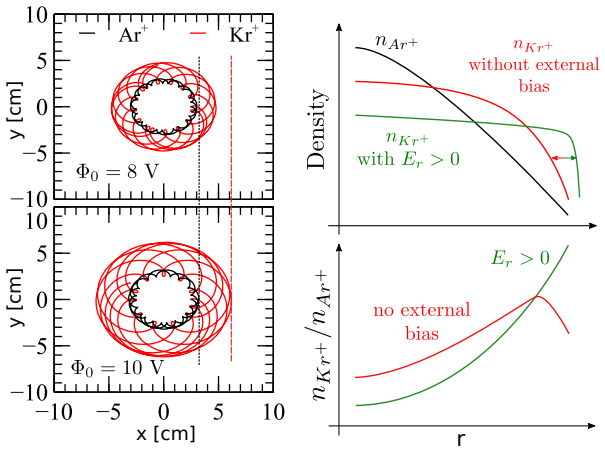

(a) Ion orbits (b) Averaged effects

Figure 11. Illustration of differential confinement effects which could explain the evolution of spectroscopic measurements with biasing. Ions orbits (a) and averaged effects (b). The ion orbits are obtained for singly charged Ar and Kr ions, magnetic field $B = 950$ G, plasma radius $r = 10$ cm and radial electric field $E_r = 2\Phi_0 r/a^2$ with $\Phi_0 = 8$ and 10 V. Ions are initialized at $r = 2.5$ cm with $T_i = 0.03$ eV.

the ionization fraction is limited ($\sim 10\%$) and the plasma volume much smaller than the chamber volume, any effective ion separation will be largely washed out by the neutrals dynamics. Baffling could mitigate these effects, and is considered for future device upgrade.

Another option to distinguish possible ion separation effects from neutrals dynamics consists in injecting material in solid form in an argon plasma and analyze the confinement properties of these elements. For this purpose, 2 μm silica spheres were injected in the machine while operating a pure argon helicon discharge. Surprisingly, preliminary experiments in this configuration did not show visual evidence of dust in the plasma. Although further investigation is needed, including spectroscopy measurements on the added material, different explanations can be proposed for this result. First, dust might not have been released as individual 2 μm spheres, but as larger clumped grains that fell through the plasma column without ablating completely. Another possibility is that the dust became charged during or after injection, and experienced electrostatic deflections due to the plasma. Finally, the dust could have been entrained in background neutral gas flows around the plasma [52].

6. Summary

A preliminary experimental study aimed at demonstrating the key components of a high throughout plasma mass filter was carried out. In particular, the possibility to control plasma profile and rotation in a multi ion-species, high density ($n \sim 10^{19}$ m^{-3}), helicon plasma through electrode biasing was investigated.

Fast camera imaging of a pure Ar plasma shows intrinsic rotation in the ion

diamagnetic direction with rotation frequency of 2 to 3 kHz. Although different azimuthal mode numbers and density profiles are observed when varying the gas pressure ($2 - 6$ mTorr), the rotation frequency does not vary significantly, and the rotation direction remains unchanged.

Langmuir probe measurements demonstrate the possibility to modify significantly the density radial profile through end-electrode biasing. The plasma density is enhanced on-axis and presents a stronger density gradient when a positive potential gradient is imposed on the electrodes. Conversely, a hollow density profile is formed when a negative potential gradient is set on the electrodes. In parallel, floating potential profile analysis reveals that the sign of the potential radial gradient imposed at the electrodes is locally recovered in the plasma in the mid-plane of the machine. With this result, the density variations might be explained in terms of single particle orbits and rotation stability.

Spatially resolved emission spectroscopy measurements confirm the plasma density profile evolution with biasing inferred from Langmuir probe measurements. Further analysis shows possible evidence of differential confinement effects. In a Ar/Kr plasma, the ratio of Kr ion to Ar ion line intensities is shown to fall off off-axis when a negative radial electric field is imposed on the electrodes, whereas this ratio remains constant or even increases slightly in the same off-axis region when a positive radial electric field is imposed.

While the results presented in this paper are encouraging, unequivocal evidence of plasma mass separation resulting from biasing controlled rotation remains to be provided. For this purpose, proper measurements of the electron temperature radial profile as well as improved spatial resolution of the spectroscopic measurements appear highly desirable. In addition, combining information on plasma rotation obtained from Mach probe measurements to density and plasma potential profiles would offer more insights into the mechanism leading to mass separation in this device.

Acknowledgments

The authors would like to thank Hantao Ji and Yevgeny Raitses for constructive discussions, as well as Darrell DiCicco, David Cylinder, Enrique Merino and Andrew Carpe for their help.

This work was supported by US DOE under contract DE-AC02-09CH11466.

References

[1] Lawrence E O 1958 Calutron system
[2] Lehnert B 1971 *Nuclear Fusion* **11** 485– ISSN 0029-5515 URL http://dx.doi.org/10.1088/0029-5515/11/5/010
[3] Bonnevier B 1966 *Ark. Fys.* **33** 255
[4] Krishnan M, Geva M and Hirshfield J L 1981 *Phys. Rev. Lett.* **46** 36–38 URL http://dx.doi.org/10.1103/PhysRevLett.46.36
[5] Grossman M W and Shepp T A 1991 *IEEE Transactions on Plasma Science* **19** 1114–1122 ISSN 0093-3813 URL http://dx.doi.org/10.1109/27.125034
[6] Rax J M, Robiche J and Fisch N J 2007 *Phys. Plasmas* **14** 043102–8 URL http://dx.doi.org/10.1063/1.2717882
[7] Freeman R, Agnew S, Anderegg F, Cluggish B, Gilleland J, Isler R, Litvak A, Miller R, O'Neill R, Ohkawa T, Pronko S, Putvinski S, Sevier L, Sibley A, Umstadter K, Wade T and Winslow D 2003 *AIP Conf. Proc.* **694** 403–410 URL http://dx.doi.org/10.1063/1.1638067
[8] Gueroult R, Hobbs D T and Fisch N J 2015 *Journal of Hazardous Materials* **297** 153–159 ISSN 0304-3894 URL http://dx.doi.org/10.1016/j.jhazmat.2015.04.058

[9] Timofeev A V 2014 *Physics-Uspekhi* **57** 990– ISSN 1063-7869 URL http://dx.doi.org/10.3367/UFNe.0184.201410g.1101

[10] Gueroult R and Fisch N J 2014 *Plasma Sources Science and Technology* **23** 035002– ISSN 0963-0252 URL http://dx.doi.org/10.1088/0963-0252/23/3/035002

[11] Ohkawa T and Miller R L 2002 *Phys. Plasmas* **9** 5116–5120 URL http://dx.doi.org/10.1063/1.1523930

[12] Fetterman A J and Fisch N J 2011 *Phys. Plasmas* **18** 094503–3 URL http://dx.doi.org/10.1063/1.3631793

[13] Gueroult R, Rax J M and Fisch N J 2014 *Physics of Plasmas* **21** 020701 URL http://dx.doi.org/10.1063/1.4864325

[14] Gueroult R and Fisch N J 2012 *Phys. Plasmas* **19** 122503–6 URL http://dx.doi.org/10.1063/1.4771674

[15] Shinohara S, Takechi S, Kaneda N and Kawai Y 1997 *Plasma Physics and Controlled Fusion* **39** 1479– ISSN 0741-3335 URL http://dx.doi.org/10.1088/0741-3335/39/9/013

[16] Miljak D G and Chen F F 1998 *Plasma Sources Science and Technology* **7** 537– ISSN 0963-0252 URL http://dx.doi.org/10.1088/0963-0252/7/4/011

[17] Biloiu I A and Scime E E 2010 *Physics of Plasmas* **17** 113508 URL http://dx.doi.org/10.1063/1.35058221.3505822

[18] Biloiu I A and Scime E E 2010 *Physics of Plasmas* **17** 113509 URL http://dx.doi.org/10.1063/1.3505823

[19] Fetterman A J and Fisch N J 2011 *Phys. Plasmas* **18** 055704–4 URL http://dx.doi.org/10.1063/1.3567417

[20] Shinohara S, Matsuoka N and Matsuyama S 2001 *Physics of Plasmas* **8** 1154–1158 URL http://dx.doi.org/10.1063/1.1350663

[21] Gilmore M, Xie S, Yan L, Watts C and Lynn A 2009 Chaos, intermittency, and sheared flow dynamics under biasing and boundary condition changes in a magnetized laboratory plasma *Proceedings of the 36th EPS Conference on Plasma Physics*

[22] Gilmore M, Hayes T R, Xie S and Yan L 2011 Flow profile changes and fluctuation suppression in a large scale helicon plasma with electrode biasing *Proceedings of the 38th EPS Conference on Plasma Physics*

[23] Zhou S, Heidbrink W W, Boehmer H, McWilliams R, Carter T A, Vincena S, Friedman B and Schaffner D 2012 *Physics of Plasmas* **19** 012116 URL http://dx.doi.org/10.1063/1.3677361

[24] Schaffner D A, Carter T A, Rossi G D, Guice D S, Maggs J E, Vincena S and Friedman B 2012 *Phys. Rev. Lett.* **109** 135002– URL http://dx.doi.org/10.1103/PhysRevLett.109.135002

[25] Tsushima A, Mieno T, Oertl M, Hatakeyama R and Sato N 1986 *Phys. Rev. Lett.* **56** 1815–1818 URL http://dx.doi.org/10.1103/PhysRevLett.56.1815

[26] Tsushima A and Sato N 1991 *J. Phys. Soc. Jpn.* **60** 2665–2672 ISSN 0031-9015 URL http://dx.doi.org/10.1143/JPSJ.60.2665

[27] Shinohara S and Horii S 2007 *Japanese Journal of Applied Physics* **46** 4276– ISSN 1347-4065 URL http://dx.doi.org/10.1143/JJAP.46.4276

[28] Maloney P, Foley J and Levinton F 2006 Lif-mse diagnostics *Proceedings of the 48th Meeting of the APS Division of Plasma Physics* JP1.027

[29] Foley E L and Levinton F M 2006 *Review of Scientific Instruments* **77** 10F311 URL http://dx.doi.org/10.1063/1.2219432

[30] Foley E L and Levinton F M 2010 *Journal of Physics: Conference Series* **227** 012007– ISSN 1742-6596 URL http://dx.doi.org/10.1088/1742-6596/227/1/012007

[31] Roquemore A, John B, Friesen F, Hartzfeld K and Mansfield D 2011 *Fusion Engineering and Design* **86** 1355–1358 ISSN 0920-3796 URL http://dx.doi.org/10.1016/j.fusengdes.2011.02.053

[32] Shinohara S, Takechi S and Kawai Y 1996 *Japanese Journal of Applied Physics* **35** 4503– ISSN 1347-4065 URL http://dx.doi.org/10.1143/JJAP.35.4503

[33] Burin M J 2003 *On Structure Formation and the Transition to Turbulence in a Magnetized Plasma Column* Ph.D. thesis University of California San Diego

[34] Lynn A G, Gilmore M, Watts C, Herrea J, Kelly R, Will S, Xie S, Yan L and Zhang Y 2009 *Review of Scientific Instruments* **80** 103501 URL http://dx.doi.org/10.1063/1.3233938

[35] Scime E E, Keiter P A, Balkey M M, Kline J L, Sun X, Keesee A M, Hardin R A, Biloiu I A, Houshmandyar S, Chakraborty Thakur S, Carr J J, Galante M, McCarren D and Sears S 2015 *Journal of Plasma Physics* **81** 345810103 URL http://dx.doi.org/10.1017/S0022377814000890

[36] Sudit I D and Chen F F 1994 *Plasma Sources Science and Technology* **3** 162– ISSN 0963-0252 URL http://dx.doi.org/10.1088/0963-0252/3/2/006

[37] Chen F F 2012 *Plasma Sources Science and Technology* **21** 055013– ISSN 0963-0252 URL http://dx.doi.org/10.1088/0963-0252/21/5/055013
[38] Scime E, Hardin R, Biloiu C, Keesee A M and Sun X 2007 *Physics of Plasmas (1994-present)* **14** – URL http://dx.doi.org/10.1063/1.2716687
[39] Light A D, Thakur S C, Brandt C, Sechrest Y, Tynan G R and Munsat T 2013 *Physics of Plasmas* **20** 082120 URL http://dx.doi.org/10.1063/1.4818148
[40] Hershkowitz N 1989 3 - how langmuir probes work *Plasma Diagnostics* ed Flamm O A L (Academic Press) pp 113–183 URL http://dx.doi.org/10.1016/B978-0-12-067635-4.50008-9
[41] Light M, Chen F F and Colestock P L 2001 *Physics of Plasmas (1994-present)* **8** 4675–4689 URL http://dx.doi.org/10.1063/1.1403415
[42] Schroder C, Grulke O, Klinger T and Naulin V 2005 *Physics of Plasmas (1994-present)* **12** – URL http://dx.doi.org/10.1063/1.1864076
[43] Tynan G R, Holland C, Yu J H, James A, Nishijima D, Shimada M and Taheri N 2006 *Plasma Physics and Controlled Fusion* **48** S51– ISSN 0741-3335 URL http://dx.doi.org/10.1088/0741-3335/48/4/S05
[44] Hardin R, Sun X and Scime E E 2004 *Review of Scientific Instruments* **75** 4103–4105 URL http://dx.doi.org/10.1063/1.1787168
[45] Thakur S C, Brandt C, Light A, Cui L, Gosselin J J and Tynan G R 2014 *Review of Scientific Instruments* **85** 11E813 URL http://dx.doi.org/10.1063/1.4890250
[46] Antar G Y, Yu J H and Tynan G 2007 *Physics of Plasmas* **14** 022301 URL http://dx.doi.org/10.1063/1.2424886
[47] Oldenburger S, Brandt C, Brochard F, Lemoine N and Bonhomme G 2010 *Review of Scientific Instruments* **81** 063505 URL http://dx.doi.org/10.1063/1.3442029
[48] Bai K H, Chang H Y and Uhm H S 2001 *Applied Physics Letters* **79** 1596–1598 URL http://dx.doi.org/10.1063/1.1404135
[49] Lieberman M A and Lichtenberg A J 1994 *Principles of Plasma Discharge for Materials Processing* (John Wiley & Sons)
[50] Shinohara S, Matsuoka N and Yoshinaka T 1999 *Japanese Journal of Applied Physics* **38** 4321– ISSN 1347-4065 URL http://dx.doi.org/10.1143/JJAP.38.4321
[51] Matsuyama S and Shinohara S 2001 *Journal of Plasma and Fusion Research SERIES* **4** 528–531 URL http://www.jspf.or.jp/JPFRS/index_vol4-5.html
[52] Krasheninnikov S I and Smolyakov A I 2003 *Physics of Plasmas* **10** 3020–3021 URL http://dx.doi.org/10.1063/1.1579692

PPPL PRINCETON PLASMA PHYSICS LABORATORY

Princeton Plasma Physics Laboratory
Office of Reports and Publications

Managed by
Princeton University

under contract with the
U.S. Department of Energy
(DE-AC02-09CH11466)

P.O. Box 451, Princeton, NJ 08543
Phone: 609-243-2245
Fax: 609-243-2751

E-mail: publications@pppl.gov

Website: http://www.pppl.gov